Investigation of the Added Utility of Different SST products in Prediction of Floods with WRF-Hydro Modeling System over Eastern Black Sea and Mediterranean Regions

Berina Mina Kilicarslan [1], Ismail Yucel [1], Heves Pilatin [2], Eren Duzenli [1], and Mustafa Tugrul Yilmaz [1]

[1] Department of Civil Engineering, Middle East Technical University, Ankara, Turkey

[2] Earth System Science Department, Graduate School of Natural and Applied Sciences, Middle East Technical University, Ankara, Turkey

Abstract (up to 300 words)

In this study, the impact of integrating four different sea surface temperatures (SST) datasets on the accuracy of the Weather Research and Forecasting (WRF)-Hydro system to simulate hydrological response during two catastrophic flood events triggered by the changes in SST is investigated. The selected events occurred over Eastern Black Sea (EBS) and Mediterranean (MED) regions of Turkey, where complex geographical characteristics exist and flash flood occurrences are associated with climatic conditions. Three time-varying and high-resolution external SST products (GHRSST, Medspiration, and NCEP-SST) and one coarse-resolution SST product (ECMWF-SST and GFS-SST for EBS and MED regions, respectively) already embedded in the initial and boundary condition dataset of WRF model are used in deriving near-surface weather variables through WRF. Using these meteorological inputs, the flood hydrographs of topographically complex small catchments located over EBS and MED regions are derived by a calibrated WRF-Hydro model coupled one way with WRF 3-km nest domain. After the proper event-based calibration performed to the WRF-Hydro using hourly and daily streamflow data of small catchments in both regions, model simulations for independent SST events are conducted to assess the impact of SST-triggered precipitation on simulated extreme runoff. The calibrated model over both regions revealed significant improvement in flood hydrographs. Some localized and temporal differences in the occurrence of the flood events with respect to observations depending on the SST

representation are noticeable. The high-resolution SST dataset cases (Medspiration and GHRSST) show error reduction up to 20% and increase in correlation from 0.3 to 0.8 with respect to the coarse SST in simulated runoffs of the EBS region. The error reduction reached 35% after the calibration. The same high-resolution SST data revealed the exact match with the observed runoff peak after 100 m^3/s reductions obtained with calibration in the MED region.

Keywords: WRF-Hydro, WRF, Calibration, Sea Surface Temperature, GHRSST, Medspiration, NCEP-SST, ECMWF-SST, GFS-SST

1. INTRODUCTION

Floods have been considered as one of the most threatening catastrophes causing human casualties and substantial economic losses. Over the last decade, an increase in the frequency of flood events has been observed. Climate model studies and numerical observations show that warming climate results in increased water vapor input into the atmosphere; consequently, the warming causes an uneven distribution of increase or decrease in the number of rainfall events that occurred worldwide. Even if the total amount of annual precipitation is expected to decrease over many regions, increased atmospheric vapor load might trigger the occurrence of more severe rainfall events. (Trenberth, 1999; Allen & Ingram, 2002). Hence, the expected increase in the intensity of the extreme precipitations implies the impact and the magnitude of the flood events might be exacerbated in time with the changing climate (Hirabayashi et al., 2013).

The heavy precipitation events and forecasting their spatial distribution are among the most significant elements of an accurate flood forecast (Shih, Chen, & Yeh, 2014; Yucel & Onen, 2014). Another critical element is the reliable forecast of the hydrological response resulting from heavy precipitation events (Ryu et al., 2017). In this context, the application of a hydrometeorological modeling framework that can integrate atmospheric and hydrological models are started to be used commonly in practice for flood forecasting (Kunstmann & Stadler, 2005). Accordingly, accurate short-term predictions of runoff inherently require well-calibrated accurate hydrological model and accurate short-term predictions of atmospheric variables (e.g., precipitation and temperature) driving this hydrological model.

Selection of the numerical weather prediction (NWP) model and the datasets driving its boundary and initial conditions have profound effect over the accuracy of the short-term predictions of the atmospheric forcing datasets; hence, better operational flood forecasts clearly require improved NWP predictions. Such NWP simulations are particularly impacted from the sea surface temperature (SST) state, as oceans/seas supply significant amount of both energy and water that the state of the atmospheric forcing variables are heavily impacted. Additionally, NWP simulations are significantly impacted from the orography, commonly exist over regions with complex topography. Accordingly, studies focusing on more accurate operational flood forecasts particularly near the coastal regions with complex topography require a land-ocean-atmosphere coupled system to better reflect variability in all elements of the water and the energy balances as well as for accurate parameterization of the

land-surface to better benefit from the input atmospheric forcing dataset. The interactions between air and sea influence the intensity of flood events, especially over the coastal areas. In the last decade, there is an increasing trend in the number of studies focusing on the effect of SST over the formation of heavy precipitation, particularly over Eastern Black Sea (EBS) and Mediterranean (MED) regions. Several studies pointed out that there is a significant relationship between SST variations and convective extremes. Lebeaupin, Ducrocq, and Giordani (2006) state that higher SST increases the moisture content in the air and warms the low level of the atmosphere. This results in stronger convection and higher precipitation totals over Southern France. Miglietta, Mazon, Motola, and Pasini (2017) highlighted that even variations of SST in order of ±1 K would have dramatically and nonlinearly changed the intensity of the supercell developed over the Ionian Sea. Senatore, Mendicino, Knoche, and Kunstmann (2014) have found that for the simulations carried out in Calabria, Italy, while the SST effect on long-term simulations identified as small, it significantly affects the individual heavy precipitation events. Following this study, it is shown that the improved representation of SST fields has a not negligible impact on simulation of the atmospheric boundary layer processes and flow dynamics (Senatore, Furnari, & Mendicino, 2020). Camera, Bruggeman, Zittis, Sofokleous, and Arnault (2020) highlights that the importance of modelled precipitation with high-resolution for flood forecast especially over small Mediterranean basins in Cyprus. According to Meredith, Maraun, Semenov, and Park (2015), a gradual increase in SST is expected to a sudden amplification of convective precipitation extremes over the Black Sea coastal regions. Studies performed in the Anatolian Peninsula agreed that the SST variations play a key role in heavy precipitation events (Bozkurt & Sen, 2011; Turuncoglu, 2015; Baltaci, 2017). Despite its significance and impact over the accuracy of the runoff forecasts, the number of studies inter-comparing the impact of different SST input datasets over the accuracy of the predicted runoff has remained limited so far (McCabe & Wolock, 2008; Chen, Wang, Xue, & Sun, 2009 ; Senatore et al., 2020).

A fully distributed, physical-based, multi-scale hydrometeorological modeling system, the WRF-Hydro system developed by the U.S. National Center for Atmospheric Research (NCAR) is developed to investigate critical water issues, including flash flood forecasting applications. Allowing to run both in uncoupled (one way from the atmosphere to land) mode and fully-coupled (two-way) mode (Gochis et al., 2020), this modeling system links the atmospheric and the hydrological processes. Overall, WRF-Hydro system is designed as a framework to couple WRF (i.e., a NWP model) with a hydrological extension that enables

simulation of land surface states and fluxes, including surface overland flow, saturated subsurface flow, and channel routing and vertical energy fluxes between land and atmosphere through physics-based and conceptual approaches. Despite many studies have been performed so far investigating the performance and application of the WRF-Hydro model (Kerandi et al., 2018; Wehbe et al., 2019; Varlas et al., 2019; Sun et al., 2020), not many studies have investigated the impact of various SST sources over the predictions of runoff. Among them, studies utilized high resolution SST inputs and implemented parameter calibration in prediction of runoff have particularly remained limited with Senatore et al. (2020).

Surrounded by sea from three sides and having one of the most complex topography in the region, Turkey has many locations living with significant potential flood threats produced by the meteorological, hydrological, and topographical differences. EBS and MED regions of Turkey are among the most vulnerable regions in terms of flood risk in the Anatolian peninsula (Gurer, 1998; Gurer & Ucar, 2009; Duzenli, Yucel, Pilatin, & Yilmaz, 2020). Over the EBS and MED coasts, the mountains parallel to the shore act as a barrier to humid air currents and cause heavy precipitation events combined result of frontal, convective, and orographic lifting effect. Particularly over the EBS region, mountains rise above 3000 m. Due to small basin structures and steep rocky characteristics, river systems can react quickly to moderate precipitation events and cause flash floods (Gurer & Ucar, 2009; Eris & Agiralioglu, 2018).

The main goal of this study is to evaluate the impact of four different SST products on the accuracy of the hydrological response of WRF-Hydro model performance throughout the selected period of simulations over two different regions in Turkey (EBS and MED). Calibration of the WRF-Hydro model using the WRF model meteorological forcing data with observed precipitation is performed for 3 and 4 selected basins located in EBS and MED regions, respectively. Thereby, the accuracy of the WRF-Hydro model predictability is assessed not only with SST product sensitivity but also with the selected physical parametrizations over EBS and MED regions. Three different heavy precipitation events for each basin in MED and EBS regions were selected for the calibration process. The calibrated parameter sets are used in the WRF-Hydro model simulations forced with the WRF model meteorological output created via initial and lower boundary conditions updated with different SST products. The paper is organized as follows: Section 2 describes the study area,

136 data, and details about WRF and WRF-Hydro model structures and selected model
137 configurations. Section 3 presents the results of the calibration process of the WRF-Hydro
138 model, the WRF model precipitation outputs and simulated hydrographs of the WRF-Hydro
139 model. Lastly, the related discussion and, concluding remarks, are given in Section 3 and
140 Section 4.

141

142 **2. DATA AND METHODS**

143 **2.1 Study Area and Event Description**

144 In this study, two significant SST-related heavy precipitation events that generated flash
145 flood over the EBS and MED regions are considered for analysis. The small catchments
146 located in EBS and MED regions with different climatic characteristics were selected as
147 study areas. Nested 3-km WRF domains (d02) covering the EBS and MED regions, selected
148 basins together with their channel networks, location of both meteorological and stream
149 gauge stations are shown in Figure 1.

150 EBS region is located in the North-Eastern part of Turkey, where the Eastern Black Sea
151 Mountain ranges lie parallel to the Black Sea. These mountain ranges rise to more than 3000
152 m above mean sea level and result in complex topography and steep-sloped characteristics
153 (Eris & Agiralioglu, 2018). The region exhibits a humid climate and receives rainfall
154 throughout the year (Turkes, 1996). It has the highest mean annual recorded precipitation,
155 which exceeds 2200 mm in Turkey (Baltaci, 2017). Due to these topographical and
156 meteorological factors, the EBS region is prone to heavy precipitation and flood events.

157 MED region has typically Mediterranean climate prevailing humid and semi-humid
158 subtropical characteristics with a rainy winter/spring and a severe hot dry summer (Turkes,
159 1996). The precipitation amount of the region is more than 1000 mm, and in many points, it
160 exceeds 2000 mm (Turkes, 1996; Eris & Agiralioglu, 2018). MED region prevails dry sub-
161 humid climatic conditions, with the Konya Plain having a semi-arid climate. Mean annual
162 precipitation is 800 mm over the MED coasts, and it increases up to 1500 mm over the
163 Taurus Mountains (Turkes, 1996; Turkes, 1999). Details of air masses affecting the regions
164 are described by Duzenli et al. (2020). The Taurus Mountains trims the coasts of the region in
165 parallel and acts as a barrier for the moist air coming from the sea. Similarly, this barrier

166 effect is observed over the EBS region. Therefore, typical topographic characteristics and sea
167 effect point out that the strong orographic lifting dependency and elevated heat sources for
168 convective initiation exist in both regions (Duzenli et al., 2020). Since high SST increases the
169 moisture content in the air, it has a critical role in the occurrence of flood events in such
170 regions located in coastal areas with complex topography.

171 [Insert Figure 1]

172 Depending on the meteorological observation dataset provided by the Turkish General
173 Directorate of Meteorology (GDM), the peak hourly precipitation amount that occurred on 24
174 August 2015 over the EBS region is recorded as 32.4 mm at Artvin-Arhavi, while total 135
175 mm of precipitation accumulated within 24-hours, which resulted in 11 fatalities, and
176 significant economic losses (Baltaci, 2017). On the other hand, for the MED event occurred
177 on 16 December 2018, the peak hourly precipitation was recorded as 53.1 mm at Antalya-
178 Ovacik station, while the total daily precipitation amount was 651.7 mm at the same station.
179 This event was registered as the highest precipitation record measured in Turkey (Kaya,
180 Guler Altan, & Yorganci, 2019). This value is almost three times higher than the monthly
181 average precipitation in December (265.3 mm) for Antalya city. The precipitation system for
182 the event that occurred during the summer season over the EBS region shows typical
183 convective system characteristics, whereas the characteristics of frontal systems are dominant
184 for the event that occurred over the MED region during the winter season (Pilatin, 2020).

185 Over the EBS region, the drainage area of the D22A049 stream gauge and its sub-basins
186 (D22A079 and D22A089) located in Arhavi province and the drainage area of the D22A147
187 stream gauge in Hopa province are selected as study basins while the drainage area of
188 D08A071, D09A095, and E08A008 stream gauges are selected study basins over MED
189 region for WRF-Hydro Model (Figure 1 and Table 1). The streamflow observations from 7
190 stream gauge stations are provided by the State Hydraulic Works (SHW) of Turkey.
191 Streamflow is provided as an average daily record in m^3/s at every selected gauging station
192 and events except for D22A049 and D08A071; it is provided as an hourly record for the
193 events that occurred after 2016 (Table 1).

194 [Insert Table 1]

195 **2.2 WRF Model**

In this study, the Advanced Research WRF model version 4.0 developed by NCAR is used to reproduce the meteorological forcing data of the WRF-Hydro model for the selected heavy precipitation events (Skamarock et al., 2019). Two-way nesting configuration is applied for the model with spatial resolution specified at 9-km for the outer domain (d01) and 3-km for the inner domain (d02). The outer domain as shown in Figure 1 extends 23.5°E-47.5°E;34.5°N- 43.5°N, and contains 232 × 111 grid points. Also, the inner domain over the MED region is placed between 47.5°N – 32.4°N, 34.5°E – 36.4°E coordinates with 73 × 88 grid points, while over the EBS region, it is placed between 47.5°N – 41.6°N, 23.5°E – 36.9°E coordinates with 136 × 52 grid points.

In this study, two different Global Circulation Models (GCMs) are selected as initial and boundary conditions to be used in the WRF model. The Global Forecasting System (GFS) forecast dataset is used over the MED region, while The European Centre for Medium-Range Weather Forecasts (ECMWF) ERA5 Re-analysis dataset is used over EBS region simulations (ECMWF, 2020; NOAA, 2015). In addition to the native (not updated daily) SST fields of GCMs, SST fields are updated with the three different external datasets. These are 1) Medspiration Level 4 Ultra-High-Resolution Foundation Sea Surface Temperature (CERSAT, 2012); 2) The Group for High-Resolution Sea Surface Temperature Level 4 Ultra-High Resolution (GHRSST) (Team GHRSST, 2010a; Team GHRSST, 2010b); 3) Real-Time, Global, Sea Surface Temperature (RTG_SST_HR) SST represented by the National Centers for Environmental Prediction (NCEP), National Oceanic and Atmospheric Administration (NOAA) and Marine Modeling and Analysis Branch (MMAB) (NCEP and NOAA, 2014). From here on, these three products will be referred as Medspiration, GHRSST, and NCEP. The optimum physics parametrization together with initial and boundary condition datasets specified for this nest WRF model configuration in both regions is determined by Duzenli et al. (2020) and Pilatin (2020). As documented in Duzenli et al. (2020), ERA5 Reanalysis data revealed the better performance in determining the initial and boundary conditions for the EBS region while GFS forecast data was found to be most appropriate for the MED region. Therefore, the corresponding SST product from these two datasets for the relevant region is used as not updated and coarse-resolution SSTs (i.e. ECMWF-SST for EBS and GFS-SST for MED). For the sensitivity analysis of SST products, time-varying and high-resolution external three different SST datasets are selected to use in WRF model. With this, both the effect of updated SST dataset and the effect of different SST products on flood events are examined.

SST datasets considered in this study are replaced with the native (not updated) SST fields available in WRF initial and lower boundary conditions. GHRSST is the first SST dataset used in this study with 0.01° spatial resolution. This dataset is provided in the highest spatial resolution among the others. Medspiration SST dataset is also included as another SST product with a horizontal resolution of 0.022°. Lastly, the NCEP SST dataset with a relatively coarse spatial resolution (with 0.083°) is added for the SST sensitivity analysis. In addition to their high spatial resolution features, all SST datasets are provided on a daily basis. All datasets are considered as satellite-derived SST datasets archived on a daily basis, except NCEP SST utilizes the model forecasts with satellite and in-situ observations (Pilatin, 2020). SST analysis of the WRF model for predicting these two heavy precipitation events were carried out by Pilatin (2020). Table 2 gives information about the initial and boundary conditions, SST dataset, and WRF model run periods corresponding to each study region.

[Insert Table 2]

2.3 WRF-Hydro Model

This study operates the WRF-Hydro model version 5.1.1. configured in an uncoupled way over the nested domain (d02) of the WRF model. Noah–Multi Parameterization (Noah-MP) is selected for the model configuration as the land surface model (LSM). In model physics options, surface overland and subsurface routing modules are activated for the whole domains, whereas the channel routing module is only activated for the study basins. The baseflow bucket model is also activated with the pass-through option. Detailed descriptions of WRF-Hydro model structure and routing modules are available in (Gochis et al., 2020). Meteorological forcing input with hourly temporal resolution from the WRF model has a horizontal resolution of 3-km, same with the Noah-MP LSM inside WRF-Hydro model. After the moisture states are calculated for the land surface column, the LSM grid disaggregates into the high-resolution routing grids which have the 250-m horizontal resolution for both study regions. High-resolution routing layers are produced from a hydrologically conditioned digital elevation model (DEM) from the Hydrological Data and Maps Based on Shuttle Elevation Derivatives at Multiple Scales (HydroSHEDS) of Lehner, Verdin, and Jarvis (2008) by regriding DEM (to 250-m) using the WRF-Hydro Pre-Processing toolbox in the GIS environment.

In calibration simulations of the WRF-Hydro model, among meteorological inputs derived from WRF model the hourly precipitation field is updated by the observed precipitation. The observed precipitation fields are created by interpolating the hourly in-situ measurements from meteorological gauges distributed over the regions through Inverse Distance Weighting (IDW) method. Based on streamflow data availability, model calibration is done for three events for each basin (7 basins in total, see Table 1), and the SST events are used independently to validate the calibrated parameter set in terms of the performance of the WRF-Hydro model. Calibration of the model is manually employed with a step-wise approach as described in Yucel, Onen, Yilmaz, and Gochis (2015). In the first step, parameters controlling the hydrograph volume called infiltration factor (REFKDT), surface retention depth (RETDEPRT), and deep drainage coefficient (SLOPE) are calibrated. Surface roughness coefficient (OVROUGHRT), channel Manning roughness coefficient (MANN), and saturated hydraulic conductivity factor (LKSATFAC) being considered as parameters controlling hydrograph shape (temporal distribution and peak timing) are calibrated in the second step. Similar procedure is commonly adopted for the calibration of WRF-Hydro in terms of water balance and its distribution (Yucel et al., 2015; Senatore et al., 2015; Naabil, Lamptey, Arnault, Kunstmann, & Olufayo, 2017; Yang, Yuan, & Yu 2018). Some parameters (REFKDT, SLOPE, MANN) are defined in tabular value format considered as global values over the domain. Others are defined as pixel specific (RETDEPRT, OVROUGHRT, LKSATFAC) that enables to change parameter value only for each basin.

Statistical measures are implemented between observed and simulated discharge for the model accuracy evaluation, namely bias, root mean square error (RMSE), and correlation coefficient (RR) to find the best parameter value among the different events for each basin. Bias represents the degree of overestimation and underestimation in hydrograph volume. RR reflects the linear relationship between observed and modelled flow and calculates the capturing performance of the timing and shape of the hydrograph. Besides, RMSE is sensitive to both the shape and the volume of the hydrograph (Moriasi et al., 2007; Gupta, Kling, Yilmaz, & Martinez, 2009). This statistical evaluation is performed based on hourly or daily time steps depending on the available temporal resolution of streamflow data of selected stream gauges.

3. RESULTS

3.1 Calibration of the WRF-Hydro Model

A representative analysis for hourly calibration of selected parameters within the WRF-Hydro model is shown in Figure 2. In this figure, first column (a-f) represents the calibration results of the event occurred between 10/19/2016 to 10/29/2016 at D22A049 basin located over EBS region while the second column (g-l) belongs to the event occurred between 03/07/2017 to 03/17/2017 at basin D08A071 located over MED region. Two more additional events belong to each of these two catchments are also used in the calibration process (Table 1). Table 3 and Table 4 show the average statistical measures calculated for the WRF-Hydro model set up with default parameter set and for the simulation of selected parameter value at the end of the calibration of each parameter for each catchment considered over EBS region and over MED region, respectively.

[Insert Figure 2]

[Insert Table 3]

[Insert Table 4]

Depending on the step-wise approach, the calibration procedure starts with the group of parameters controlling the hydrograph volume. Initially, calibration of the REFKDT parameter (default value of 3.0) is performed with the parameter values between 0.5 and 5.0 with 0.5 increments. Figure 2(a) and Figure 2(g) show the results of D22A049 and D08A071 basins, respectively. It can be inferred as the higher the REFKDT value lower the infiltration capacity of the soil column, in turn, the higher the hydrograph volume. According to the statistics and comparison with the calibration hydrographs based on the other two events, it is decided on to select the lowest value (0.5) in the REFKDT calibration range for both basins. Though the lowest value of 0.5 is selected as the optimum value, there is still an underestimation observed in the D022A049 hydrograph volume in Figure 2(a). However, the simulated first peak in day-8 is lowered, and the simulated hydrograph is fed through the observed peak that occurred in between day-7 and day-8. On the contrary, the average bias calculated for three events (including this event) for this basin turns into 3.72 in Table 3. Same contrast is observed also in the D08A071 station. Negative bias is observed for the average of the three events (Table 4), while an overestimation is observed for the represented event in Figure 2(b) for selected REFKDT value. Overall statistic shows that REFKDT parameter seems sensitive in both regions.

Figure 2(b) and Figure 2(h) shows the calibration results of the RETDEPRTFAC parameter with the specified calibration range of 0.0-10.0 with 1.0 increment. Default RETDEPRTFAC parameter value is defined as 1.0, meaning that the initial retention depth of 1 mm on grid cells. Simulated hydrographs of both basins are not showing an apparent response to the RETDEPRTFAC parameter (Table 3 and Table 4). Since EBS and MED regions have steep and complex topographical characteristics, little water accumulation over the terrain is expected to be observed. Therefore, the optimum RETDEPRTFAC parameter value is selected as 0.0 for both basins.

As a last hydrograph volume controlling parameter, SLOPE is considered for the model calibration using values between 0.1 and 1.0 range with 0.3 increments. Similar to Wang et al. (2019), only the first class of the nine SLOPE_DATA categories represented in GENPARM.TBL is subjected to tuning. This parameter controls the openness of the bottom soil column to the conceptual bucket. According to Figure 2(c) and Figure 2(i), the parameter shows little influence on simulated hydrographs in terms of statistics The default value is selected as an appropriate SLOPE parameter value for the model in D22A049 and D08A071 basins. However, it is observed that the other calibrated events in D22A147 and D09A095 basins show improvement in RMSE and correlation coefficient with respect to the SLOPE parameter (Table 3 and Table 4).

For the second step, parameters controlling hydrograph shape and timing are considered for the calibration process. Figure 2(d) and Figure 2(j) show the results from the calibration of the OVROUGHRTFAC parameter with parameter values ranging from 0.1 to 1.0 with 0.3 increments. The OVROUGHRTFAC parameter has an impact on the speed of the infiltration excess water transmitted through the channel network grids, which affects the hydrograph volume. Default surface roughness values are defined depending on the land use classes categorized in HYDRO.TBL. For this study, MODIS-20 category land use data is selected inside the LSM. Based on the comparison of hydrographs and statistics, the default value of OVROUGHRTFAC is found to be optimum for both basins except a selected value of 0.1 for basin D09A095 (Table 4). Parameter range between 0.4 and 0.7, the effect of tuning the parameter is not seen in the hydrograph of basin D08A071 in Figure 2(j).

Manning's Roughness scaling factor for all stream orders is calibrated with a scaling factor (MANN) within a range from 0.5 to 2.0 with 0.5 increments. MANN controls the conveyance time of the flow through the channel network, which can be interpreted as the higher MANN

values creates a slower peak and smaller hydrograph volume. Figure 2(e) and Figure 2(k) show that the highest correlation is seen for the value of 2.0; thus, scaling factor is selected as 2.0 for the MANN parameter. RMSE and correlation coefficient improvement in all basin except constant correlation coefficient is observed in D22A049 (Table 3 and Table 4).

Lastly, the LKSATFAC parameter, which affects the lateral redistribution of infiltrated water, is calibrated for the values of 10, 100, 1000 (default), and 10000, as it is shown in Figure 2(f) and Figure 2(l). It appears that LKSATFAC is the most sensitive parameter in both regions particularly for the MED region. It influences peak timing and its magnitude with a significant decrease. Based on its effect on both regions, the value of 10 is determined as the optimum value for LKSATFAC.

In Table 3, progressive improvement of RMSE and correlation coefficient is observed from the first simulation (with default parameter set) to the simulation of LKSATFAC with the value of 10 in both basins. After the calibration process is finished, correlation coefficient is increased from 0.13 to 0.56, while RMSE is reduced from 40.55 to 32.16 for D22A49. On the other hand, bias suddenly turn into negative value after the calibration stage LKSATFAC for D22A049. The effect of sudden decrease in the recession stage in Figure 2(f) is likely seen in calculated average bias in Table 3. In D22A147, significant improvement is observed in correlation coefficient (from 0.38 to 0.71) at the end of the calibration process. For D08A071 basin, an improvement is observed only in correlation coefficient, while increase of bias and RMSE values are observed after the calibration of the fifth parameter, MANN (Table 4). In D09A095 and E08A008, statistics at the end of the calibration process show an improvement compared to the model performed with default parameters set (Table 4). E08A008 exhibits no response to the RETDEPRT, SLOPE and OVROUGHRTFAC parameters. From these results, it appears that the WRF-Hydro model is considerably sensitive to the LKSATFAC parameter especially in the MED region simulations. Calibrated parameters for each basin with their default values are shown in Table 5.

[Insert Table 5]

3.2 Precipitation evaluation for each SST case

Figure 3 (a) and (b) show the comparison between observed and WRF-derived basin-averaged precipitation time series of each SST case for D22A147 and D08A071 basins, respectively. On the other hand, Table 6 shows the statistical measures calculated for each SST case in both basins. In Figure 3 (a), the precipitation time series are represented from 08/17/2015 00:00:00 UTC to 08/27/2015 00:00:00 UTC with a 241-hours. The maximum precipitation amount for this basin is recorded as 26.3 mm for the 178th hour, which corresponds to 08/24/2015 09:00:00 UTC. However, the maximum precipitation for the EBS region for this event was recorded as 32.4 mm at 08/24/2015 00:00:00 UTC. The spatial patterns of this precipitation amount measured in the meteorological station towards the D22A049 basin, not in the range of D22A147 basin boundaries. Nevertheless, as shown in Figure 3 (a), the effect of event center on the basin-average precipitation of the D22A147 basin is still observed, and it is recorded as 16.1 mm at the 169th hour, which corresponds to the event peak time for the whole EBS region. Also, it can be interpreted that simulations performed with different SST datasets are able to catch the general pattern of the observation, except they generate the primary peak couple of hours earlier than the observation peak. However, notwithstanding the poor statistical measures (low correlation of 0.01-0.03 and high RMSE of 3.19-5.30) in Table 6, it can be depicted that using an external high-resolution SST dataset still improves the accuracy of the simulated precipitation, especially for Medspiration. Besides, GHRSST simulation overestimates the observed peak precipitation. Other simulated peaks are lower than the GHRSST simulation, but they are closer to the observed peak.

In Figure 3 (b), the basin-averaged precipitation time series are represented from 12/10/2018 00:00:00 UTC to 12/20/2018 00:00:00 UTC with a 241-hours. Peak time and precipitation magnitude of the ten-day run period for the whole MED region is recorded as 53.1 mm at 162th hour (at 12/10/2018 17:00:00 UTC). The maximum basin-average precipitation value of 15.7 mm is calculated at the same time step for the D08A071 basin. Overall, simulated precipitations show nearly the same trend with the observation with minor overestimations with positive precipitation bias. Nonetheless, it appears that external SST simulations are able to improve the precipitation volume with reduced bias. Modest delays in peak time (1-2 hours) are observed for GFS SST, GHRSST, and NCEP SST simulations, while Medspiration precipitation catches the exact peak time. Comparing with the observed peak precipitation amount, simulation performed with the GFS SST creates the highest overestimation around 17 mm, and in terms of model run period, it creates a positive bias value of 0.56 (Table 6).

Medspiration shows the best model performance in terms of all statistics calculated with respect to the observed precipitation compared to the rest (Table 6).

[Insert Figure 3]

[Insert Table 6]

Figure 4 shows the spatial distribution of observed precipitation and simulated precipitations from the WRF model created by different SST datasets in peak day (08/24/2015) over the EBS region. Observation precipitation map is created by IDW method using the point observations of meteorological stations, as shown in Figure 4 (a). It is noteworthy that in Figure 4 GHRSST simulation shows an overestimation in spatial distribution of precipitation over the basin D22A147 compared to observed precipitation (Figure 4 (c)). Medspiration generates the closest precipitation distribution to the observation over the D22A147 basin, consistent with the previously mentioned remark that Medspiration improves the accuracy of precipitation estimates compared to native coarse-resolution SST dataset (ECMWF) in Figure 4 (d). Medspiration and GHRSST simulations also overestimate the precipitation towards the coastline, where they produce more than 140 mm of daily precipitation in Figure 4 (c and d). Besides, NCEP simulation leads to the underestimation of the simulated precipitation as shown in Figure 4 (e). On the other hand, GHRSST catches the location of observed heavy precipitation considerably among the other simulations (Figure 4 (c)).

[Insert Figure 4]

For the MED region, Figure 5 shows the spatial distribution of simulated precipitation (GFS, GHRSST, Medspiration, and NCEP) and observed one with a maximum precipitation depth of 53.1 mm at the peak hour (Figure 5 (a)). Simulation performed with GFS SST shows overestimation in terms of precipitation amount. It also misses the event location and creates the event over the sea near the coastline instead of over the land (Figure 5 (b)). Besides, simulations performed with external high-resolution SST datasets are reasonably well represented for the peak time compared to GFS simulations to catch the event location over the land. Figure 5 (c) shows that GHRSST simulation can capture the observed event location yet, it cannot generate enough precipitation and causes underestimation with a precipitation depth of 16-18 mm, which is due to the modest delay in peak time mentioned earlier. Medspiration and NCEP simulations reveal much closer precipitation predictions to the observation in terms of precipitation depth (Figure 5 (d-e)). Especially, Medspiration

simulation steps forward in generating similar precipitation depth and catching the similar hotspot of the observed events. Lastly, the spatial distribution of precipitation over the D08A071 basin for Medspiration, well matches the peak precipitation timing and amount in Figure 3 (b). Thus, Medspiration overestimates the observed precipitation by around 8 mm (the highest hourly precipitation for Medspiration simulation over D08A071 basin is 25.8 mm which corresponds to the darker orange coloring of the basin grids (Figure 5 (d)).

[Insert Figure 5]

3.3 Evaluation of the WRF-Hydro for SST events

The performance of the calibrated WRF-Hydro model is evaluated with respect to the un-calibrated model using each SST case in D22A147 and D08A071 basins. In Figure 6 (a), ECMWF SST and NCEP SST hydrographs show substantial underestimation for the peak volume of the observed hydrograph. This may due to the negative bias observed in event precipitation in Figure 3 (a) for ECMWF SST and NCEP SST simulations (They are the ones with the highest negative bias among other SST simulations.). Medspiration SST simulation creates slightly better hydrograph volume and shows better statistics compare to ECMWF SST and NCEP SST simulation. Though the GHRSST generates overestimation in precipitation and misses the event peak time for the D22A147 basin as discussed in the previous session (Figure 3 (a)), the daily mean discharge of the GHRSST simulation makes the best improvement in the discharge estimation. This is due to the fact that the WRF simulation of the GHRSST generated the most realistic amount of water volume that the D22A147 basin received on peak day (in 08/24/2015) as shown in Figure 4 (c). Therefore, the daily mean of the total water conveyed to the channel network after the water balance calculations resulted in the closest simulated discharge volume to the observed one with the lowest negative bias and RMSE values among the other simulated hydrographs (Figure 6 (a)). The bias value of the simulated hydrographs with GHRSST precipitation is reduced by -1.8 (from -10.5 to -8.7) while RMSE is reduced by 4.2 (from 20.7 to 16.5) as compared to hydrograph simulated with ECMWF precipitation (Table 7). On average, correlation coefficients increase from 0.3 for the simulated hydrograph with ECMWF SST to 0.8 for the simulated hydrographs with external SST datasets. A sharp decrease in the recession stage in the hydrographs of all simulations is observed as different from the observed hydrograph. Overall, from the statistical measures in Table 7, it can be seen that simulated hydrographs obtained from WRF model forcings derived by external high-resolution SST datasets show

478 better performance in terms of both peak timing and hydrograph volume corresponding to the
479 observed hydrograph.

480 [Insert Figure 6]

481 [Insert Table 7]

482 In Figure 6 (b), the realistic volume increase is observed in the simulated hydrographs
483 through the calibrated set of parameters in the D22A147 basin. The correlation coefficients of
484 simulated hydrographs are similar to those before calibration, except for the calibrated
485 parameter set increases to 0.4 for ECMWF simulation. Medspiration SST and NCEP SST
486 hydrographs volumes are improved, and they are way closer to the volume of observed
487 hydrograph, but their underestimation is still higher compare to GHRSST hydrograph. The
488 calibrated parameter set also substantially increases the GHRSST hydrograph volume and
489 makes it closer to the observation compare to other simulations. For GHRSST simulated
490 hydrograph, bias and RMSE is reduced by -2.5 (from -8.7 to -6.2) and 5.7 (from 16.5 to
491 10.8), respectively (Table 7). These results indicate that the GHRSST is the most
492 representative SST dataset for D22A147 basin among the other SST datasets in the way of its
493 effect on simulated hydrograph with respect to observed hydrograph and the calibration of
494 the WRF-Hydro model is also essential to further improve the model simulation, especially in
495 terms of hydrograph volume.

496 Comparison of hourly observed hydrographs and simulated hydrographs forced by four
497 different SST events in the D08A071 basin is represented in Figure 7 (a) (plotted for the last
498 six days of the model run period). Figure 7 (b) shows the equivalent plots with the set of
499 calibrated parameters for the D08A071 basin. In Figure 7 (a), hourly simulated discharge
500 patterns are well matched with the observation for external SST datasets (GHRSST,
501 Medspiration SST, and NCEP SST) simulations with the correlation coefficient values of
502 around 0.6 (Table 7). Minor delays in the primary hydrograph peak time are observed for the
503 simulated hydrographs with GHRSST and NCEP SST. They overestimate the observed
504 discharge until peak time, yet the underestimation in the falling limb stage causes negative
505 bias between -18.85 and -26.24 as shown in the Table 7. A simulated hydrograph forced by
506 the WRF model derived from GFS SST produces a substantially higher peak of 877.4 m^3/s
507 compared to the observed hydrograph and mismatches the hydrograph timing trend. The
508 overestimation in a peak discharge of this hydrograph is likely due to the positive bias in the

peak time of hourly precipitation time series of GFS SST derived precipitation simulation in Figure 3 (b). Though the GFS SST hydrograph has the lowest bias value (-7.1), it produces the highest RMSE (125.9) and lowest correlation coefficient (0.3) (Table 7). Therefore, the simulated hydrograph shows better performance in terms of peak timing and magnitude of the hydrograph with the WRF forcing updated by external high-resolution SST, consistent with that they show the closer spatial distribution of precipitation in peak time compare to observation over the D08A071 (Figure 5).

[Insert Figure 7]

Simulated hourly hydrographs with the calibrated parameter set in Figure 7 (b) represent better behavior in rising limb parts till their peak values but they worsen for their falling limb parts after model calibration. It can be interpreted that model is trying to adapt to extraordinarily high observed peak discharges (301.4 m^3/s) via calibration. This is likely the evidence for the discrepancy in statistical measures in Table 7, are getting worse after the calibration of the model. For hydrographs derived with GHR-SST and NCEP SST precipitations still exhibit a minor shift in the primary peak timing and magnitude. With a reduction of 100 m^3/s the observed peak value is greatly captured by high-resolution external SST products.

3.4. Evaluation of Rainfall-Runoff Representations

Figure 8 shows overlapped dynamic maps of accumulated precipitation simulated by the WRF model using four different SST datasets (ECMWF, GHRSST, Medspiration and NCEP) and simulated discharges on the gridded river networks corresponding to these four precipitation estimates over the EBS region for D22A49 and D22A147 basins. The D22A147 basin is located at the north-eastern part of the map, while the D22A049 is located at the center of the map. Blue dots over the maps highlight the location of outlet points (stream gauge station from Figure 1) of the basins. The first-time step in Figure 8 (a-d) shows the accumulated precipitation shortly before the start of the precipitation event and the state of the river networks of the D22A49 and D22A147 basins having the discharge at the baseflow level. In Figure 8 (f), at the second time step, the D22A147 basin receives the highest precipitation compared to others; this result is consistent with that the simulated precipitation with GHRSST generates the highest overestimation stated in the previous section. Due to the steep slope characteristics of the basins over the EBS region, it can be seen that the

precipitation is immediately conveyed (less than 1 hour) to the river network and collected to the outlet point and lead to flooding. This is clearly seen in Error: Reference source not foundFigure 8 (f) for the D22A147 basin, in Error: Reference source not foundFigure 8 (f) for the D22A049 basin, and in Error: Reference source not foundFigure 8 (g-h) for both basins. For the third time step, the river network responds with lowered discharge values and lastly returns to the baseflow since there is no significant precipitation observed at the previous time step (Figure 8 (i-l)).

[Insert Figure 8]

Figure 9 shows overlapped dynamic maps of accumulated precipitation simulated by the WRF model through using four different SST datasets (GFS, GHRSST, Medspiration, and NCEP) and simulated discharges on gridded river networks corresponding to these four precipitation estimates over the MED region for D08A071, D09A095, and E08A008 basins. The D09A095 basin is located north-easterly at the top of the map, while the D08A071 basin is located at the bottom of the D09A095 basin, and the E08A008 is located at the bottom left of the map the first-time step (02:00:00 UTC) demonstrates the precipitation event start over the basins located towards the east at which channel grids of mentioned basins are started to be filled with water. At 16:00:00 UTC, the simulated discharge amount with GFS-SST at the outlet of the D08A071 basin reaches from 142 m^3/s to 516 m^3/s as a response to the precipitation accumulated in the region for 14 hours, especially over the upstream basin (Figure 9 a, e). The precipitation event takes place towards the D09A095 basin for MED-SST simulation, and it appears that precipitated water is collected from the upper basin and conveyed to the outlet point and reaches the discharge value of 698 m^3/s (Figure 9 g). In Figure 9 (l), due to the minor delays in primary peak time discharge in hydrographs forced by precipitation input derived from GHRSST and NCEP SST, the channel grid network still on the rising limb stage with respect to the simulated hydrographs in Figure 7(b)Error: Reference source not found.

[Insert Figure 9]

4. DISCUSSION

The spatial and the temporal differences in precipitation greatly affect the accuracy of runoff simulation in terms of timing and magnitude of the peak value, and overall volume (Yucel et al., 2015; Senatore et al., 2020). Various SST products indeed resulted in different

precipitation variability both in space and time over both regions. Particularly smaller the size of the basins the greater the variability. Given the catchments are characterized with small size and complex topographical structure over both EBS and MED regions, the use of high-resolution precipitation products is critically important. In event simulations by WRF, the updates in SST through model integration are usually not activated because the variability of SST is small during a short event period. However, it is expected that changing climate causes abnormal SST changes that trigger the formation of the occurrence of heavy precipitation events (Pilatin, 2020). As stated in Bozkurt and Sen (2011), increased SST in winter shows a strong response in the atmosphere over the Mediterranean Sea while atmospheric response is very sensitive to SST over the Black Sea during the autumn and summer seasons. The daily updated SST products from GHRSST, Medspiration, and NCEP over both study regions revealed significant changes in heavy precipitation amounts with respect to the not-updated (native) SST products from GFS over MED and ECMWF over EBS. They improved the accuracy of predictions in terms of storm location, timing, and extent particularly over the MED region. High spatial representation also contributes to this improvement. As a result, the Medspiration over the MED region and GHRSST over the EBS region revealed the best basin-averaged precipitation representation that is directly relevant to the improvement in surface runoff prediction in small catchments of both study regions. The high-resolution SSTs (GHRSST and Medspiration) help resolve high variability in rainfall and its hydrologic response resulted from a typical convective system occurred in the ESB region. The calibrated WRF-Hydro model significantly highlighted the improvement provided by these two SST products over the EBS region. Even though the statistics show some degradation in runoff results after model calibration, the calibrated model indeed improved the rising limb parts of the storm hydrographs till their peak occurrence particularly for Medspiration- and GHRSST-based simulations over the MED region. Since the MED SST event produced an observed peak around 300 m^3/s, the calibration became highly sensitive to this peak value and therefore it showed a poor performance in describing the falling limb parts of the hydrographs. The effective parameter sets controlling the volume and shape of the hydrograph need to be identified prior to the operational runoff forecast to perform more accurate forecasts (Yucel et al., 2015; Senatore et al., 2015; Silver, Karnieli, Ginat, Meiri, & Fredj, 2017). Among the parameters, REFKDT, SLOPE, MANN and LKSATFAC revealed an important impact on making reliable runoff prediction in both regions but especially the saturated hydraulic conductivity parameter factor (LKSATFAC) became substantially critical over the MED region. It might be relevant to the fact that the

sub-surface geological formation of the MED region is dominantly represented by the karstic formation. With sharp and steep small catchments over the EBS, the hydrologic response is very fast and overland flow is quickly joined to the river networks and pours to the outlets within 1-h period. The high-resolution gridded rainfall-runoff coupling greatly benefits to monitor the water excess condition for a given storm over topographically complex and steeply small watersheds.

5. CONCLUSIONS

This study investigated the hydrologic response of the small catchments characterized by complex coastal orography and diverse climate to the heavy precipitation events simulated by the various SST products featured as coarse- and high-resolution, and daily updated and not updated products within the WRF model. The flood hydrographs of the heavy rainfall events are simulated using the physical-based and fully-distributed WRF-Hydro model configured with one-way coupling from WRF 3-km domain to the Hydro model. GFS over the MED region and ECMWF (ERA5) data over EBS region include their own SST values (considered as coarse resolution and not updated data sets), whereas GHRSST, Medspiration, and NCEP SST products are described as high resolution and updated external products used in both study regions. Calibration of the WRF-Hydro model is carried out for two different groups of parameters controlling hydrograph volume and shape of the hydrograph in a step-wise approach to improve the performance of the WRF-Hydro model further. The main findings of this study are listed as follows:

- Simulated precipitations updated with high-resolution SST datasets instead of native SST fields in initial boundaries of the WRF improve the precipitation accuracy with respect to observations for two events resulted from different precipitation systems. This effect varies depending on the studied region; e.g., over the MED region, better improvement is explicitly observed in terms of capturing the peak time and the precipitation depth.
- Using high-resolution and time varying SST products (Medspiration and GHRSST) is very effective in capturing the temporal and spatial changes of precipitation depth in small catchments.

- Better representation of precipitation variability via high-resolution SST also help improve the runoff predictions of small catchments located both over EBS and MED regions.
- High-resolution SST updates impact on simulated hydrograph in both regions came into prominence in terms of predicting peak discharge values more accurately by the effect of changing precipitation spatial distribution, and intensity resulted from different external SST datasets.
- Calibration of the model further improved the model statistical measures for simulated hydrographs over the EBS region, and it was observed that the hydrographs simulated over the MED region are way more sensitive to the calibration, especially in terms of peak timing and magnitude, though the statistical measures were degraded in the falling limb part of the hydrographs.
- The effect of calibrated parameters on statistics improvement was found slightly better than the SST effect over the EBS region, while over the MED region, both SST and calibration effects were found prominent in terms of hydrograph improvement capacity.
- High-resolution GHRSST and Medspiration SST stepped forward to show more significant improvement compared to other SST datasets to capture peak discharge timing and magnitude for hydrographs simulated over EBS and MED regions, respectively.

Overall, the findings of this study from the precipitation and hydrograph simulations demonstrate the potential benefit of using high-resolution SST datasets in initial and lower boundary conditions of the WRF model simulations. Under the consideration of abnormal SST changes exacerbated by changing climate, time-varying SST features should be accounted for extreme weather event evaluations in complex coastal topographical regions. Additionally, the effect of the WRF-Hydro model calibration on simulated hydrographs displays satisfactory enhancement. Such improvements are considered noteworthy in terms of early warning systems, especially regions under the significant influence of sea effect in atmospheric conditions and have a complex topographical characteristic that poses high flood risk.

ACKNOWLEDGEMENTS

We thank to GDM and SHW of Turkey for the ground-based meteorological observation and streamflow datasets, The Group for High Resolution Sea Surface Temperature for GHRSST datasets, CERSAT for Medspiration datasets, NCEP for RTG_SST datasets and GFS products, ECMWF for ERA5 products, and NCAR/NOAA for serving and improving the WRF model. This project is funded by The Scientific and Technological Research Council of Turkey (TUBITAK) [Grant Number 116Y193].

DATA AVAILABILITY

All of the datasets used in the current study can be found in the following open-source online data repositories:

GFS dataset from https://rda.ucar.edu/datasets/ds084.1/ at NCAR.

ERA5 dataset from https://cds.climate.copernicus.eu/#!/search?text=ERA5&type=dataset at ECMWF.

GHRSST dataset from https://podaac.jpl.nasa.gov/dataset/OISST_UHR_NRT-GOS-L4-MED-v2.0?ids=TemporalResolution&values=Daily&search=l4 for Mediterranean and https://podaac.jpl.nasa.gov/dataset/OISST_UHR_NRT-GOS-L4-BLK-v2.0?ids=TemporalResolution&values=Daily&search=l4 for Eastern Black Sea regions at NASA Physical Oceanography Distributed Active Archive Center (PODAAC).

Medspiration dataset from http://cersat.ifremer.fr/thematic-portals/projects/medspiration at CERSAT.

NCEP dataset from ftp://polar.ncep.noaa.gov/pub/history/sst/rtg_high_res at NCEP.

REFERENCES

Allen, M.R., & Ingram, W.J., 2002. Constraints on future changes in climate and the hydrologic cycle. *Nature.Com 419*, 225–232.

Baltaci, H., 2017. Meteorological analysis of flash floods in Artvin (NE Turkey) on 24 August 2015. *Natural Hazards and Earth System Sciences 17*, 1221–1230. https://doi.org/10.5194/nhess-17-1221-2017

Bozkurt, D., & Sen, O.L., 2011. Precipitation in the Anatolian Peninsula: Sensitivity to

691 increased SSTs in the surrounding seas. *Climate Dynamics. 36*, 711–726. https://doi.org/
692 10.1007/s00382-009-0651-3

693 Camera, C., Bruggeman, A., Zittis, G., Sofokleous, I., & Arnault, J., 2020. Simulation of
694 extreme rainfall and streamflow events in small Mediterranean watersheds with a one-
695 way-coupled atmospheric-hydrologic modelling system. *Natural Hazards and Earth*
696 *System Sciences 20*, 2791–2810. https://doi.org/10.5194/nhess-20-2791-2020

697 CERSAT, 2012. Medspiration. Available at: http://cersat.ifremer.fr/thematic-portals/projects/
698 medspiration [Accessed 7 January 2021].

699 Chen, W., Wang, L., Xue, Y., & Sun, S., 2009. Variabilities of the spring river runoff system
700 in East China and their relations to precipitation and sea surface temperature.
701 *International Journal of Climatology 29*, 1381–1394. https://doi.org/10.1002/joc.1785

702 Duzenli, E., Yucel, I., Pilatin, H., & Yilmaz, M.T., 2020. Evaluating the performance of a
703 WRF initial and physics ensemble over Eastern Black Sea and Mediterranean regions in
704 Turkey. *Atmospheric Research 248*, 105184.
705 https://doi.org/10.1016/j.atmosres.2020.105184

706 ECMWF, 2020. ERA5. Available at: https://www.ecmwf.int/en/forecasts/datasets/reanalysis-
707 datasets/era5 [Accessed 7 January 2021].

708 Eris, E., & Agiralioglu, N., 2018. Streamflow map of the Eastern Black Sea Region, Turkey.
709 *Scientia Iranica 25*, 1048–1056. https://doi.org/10.24200/sci.2017.4261

710 Gochis, D.J., Barlage, M., Cabell, R., Casali, M., Dugger, A., FitzGerald, K., … Zhang, Y.,
711 2020. The WRF-Hydro modeling system technical description, (Version 5.1.1). NCAR
712 Tech. Note 107.

713 Gupta, H. V., Kling, H., Yilmaz, K.K., & Martinez, G.F., 2009. Decomposition of the mean
714 squared error and NSE performance criteria: Implications for improving hydrological
715 modelling. *Journal of Hydrology 377*, 80–91.
716 https://doi.org/10.1016/j.jhydrol.2009.08.003

717 Gurer, I., 1998. Flood Disasters and Preventatiye Measures in Turkey. *Journal of Natural*
718 *Disaster Science 20*, 1–9.

719 Gurer, I., & Ucar, I., 2009. Flood Disasters' Inventory in Turkey in 2009. Eleventh
720 International Symposium on Water Management and Hydraulic Engineering 371–380.

721 Hirabayashi, Y., Mahendran, R., Koirala, S., Konoshima, L., Yamazaki, D., Watanabe, S., …
722 Kanae, S., 2013. Global flood risk under climate change. *Nature Climate Change 3*,
723 816–821. https://doi.org/10.1038/nclimate1911

724 Kaya, O.F., Guler, M., Altan, A., & Yorganci, I., 2019. 15-16-17 Aralık 2018 Tarihlerinde
725 Antalya İli Kemer/Ocavık Mevkiinde Görülen Aşırı Yağış Hadisesinin Aktüel Hava
726 Haritaları, Uzaktan Algılama ve Sayısal Hava Tahmin Ürünleri ile Sinoptik ve
727 Hidrolojik Analizi, in: 10. Ulusal Hidroloji Kongresi 9-12.

728 Kerandi, N., Arnault, J., Laux, P., Wagner, S., Kitheka, J., & Kunstmann, H., 2018. Joint
729 atmospheric-terrestrial water balances for East Africa: a WRF-Hydro case study for the
730 upper Tana River basin. *Theoretical and Applied Climatology 131*, 1337–1355.
731 https://doi.org/10.1007/s00704-017-2050-8

732 Kunstmann, H., & Stadler, C., 2005. High resolution distributed atmospheric-hydrological
733 modelling for Alpine catchments. *Journal of Hydrology 314*, 105–124.
734 https://doi.org/10.1016/j.jhydrol.2005.03.033

735 Lebeaupin, C., Ducrocq, V., & Giordani, H., 2006. Sensitivity of torrential rain events to the
736 sea surface temperature based on high-resolution numerical forecasts. *Journal of*
737 *Geophysical Research Atmospheres 111*, 1–19. https://doi.org/10.1029/2005JD006541

738 Lehner, B., Verdin, K., & Jarvis, A., 2008. New global hydrography derived from spaceborne
739 elevation data. *Eos* (Washington. DC). *89*, 93–94.
740 https://doi.org/10.1029/2008EO100001

741 McCabe, G.J., & Wolock, D.M., 2008. Joint variability of global runoff and global sea
742 surface temperatures. *Journal of Hydrometeorology 9*, 816–824.
743 https://doi.org/10.1175/2008JHM943.1

744 Meredith, E.P., Maraun, D., Semenov, V.A., & Park, W., 2015. Evidence for added value of
745 convection-permitting models for studying changes in extreme precipitation. *Nature*
746 *175*, 238. https://doi.org/10.1038/175238c0

747 Miglietta, M.M., Mazon, J., Motola, V., & Pasini, A., 2017. Effect of a positive Sea Surface
748 Temperature anomaly on a Mediterranean tornadic supercell. *Scientific Reports 7*, 1–8.
749 https://doi.org/10.1038/s41598-017-13170-0

750 Moriasi, D.N., Arnold, J.G., Van Liew, M.W., Bingner, R.L., Harmel, R.D., & Veith, T.L.,
751 2007. Model Evaluation Guidelines for Systematic Quantification of Accuracy in
752 Watershed Simulation. *Colombia Medica 50*, 885–900. https://doi.org/10.1234/590

753 Naabil, E., Lamptey, B.L., Arnault, J., Kunstmann, H., & Olufayo, A., 2017. Water resources
754 management using the WRF-Hydro modelling system: Case-study of the Tono dam in
755 West Africa. *Journal of Hydrology: Regional Studies 12*, 196–209.
756 https://doi.org/10.1016/j.ejrh.2017.05.010

757 NCEP, NOAA, 2014. NCEP SST Analysis. Available at:
758 https://polar.ncep.noaa.gov/sst/ophi/verification.shtml [Accessed 7 January 2021].

759 NOAA, 2015. NCEP GFS 0.25 Degree Global Forecast Grids Historical Archive Research
760 Data Archive at the National Center for Atmospheric Research, Computational and
761 Information Systems Available at: https://doi.org/10.5065/D65D8PWK [Accessed 7
762 January 2021].

763 Pilatin, H., 2020. Sensitivity and Sea Surface Temperature Analyses of WRF Model for
764 Predicting Heavy Rainfall events Observed in Eastern Black Sea and Mediterranean
765 Regions of Turkey. Master's thesis, Middle East Technical University, Turkey.

766 Ryu, Y., Lim, Y.J., Ji, H.S., Park, H.H., Chang, E.C., & Kim, B.J., 2017. Applying a coupled
767 hydrometeorological simulation system to flash flood forecasting over the Korean
768 Peninsula. *Asia-Pacific Journal of Atmospheric Sciences 53*, 421–430.
769 https://doi.org/10.1007/s13143-017-0045-0

770 Senatore, A., Furnari, L., & Mendicino, G., 2020. Impact of high-resolution sea surface
771 temperature representation on the forecast of small Mediterranean catchments'
772 hydrological responses to heavy precipitation. *Hydrology and Earth System Sciences 24*,
773 269–291. https://doi.org/10.5194/hess-24-269-2020

774 Senatore, A., Mendicino, G., Gochis, D.J., Yu, W., Yates, D.N., & Kunstmann, H., 2015.
775 Fully coupled atmosphere-hydrology simulations for the central Mediterranean: Impact

of enhanced hydrological parameterization for short and long time scales. *Journal of Advances in Modeling Earth Systems 7*, 1693–1715. https://doi.org/10.1002/2015MS000510

Senatore, A., Mendicino, G., Knoche, H.R., & Kunstmann, H., 2014. Sensitivity of modeled precipitation to sea surface temperature in regions with complex topography and coastlines: A case study for the Mediterranean. *Journal of Hydrometeorology 15*, 2370–2396. https://doi.org/10.1175/JHM-D-13-089.1

Shih, D.S., Chen, C.H., & Yeh, G.T., 2014. Improving our understanding of flood forecasting using earlier hydro-meteorological intelligence. *Journal of Hydrology 512*, 470–481. https://doi.org/10.1016/j.jhydrol.2014.02.059

Silver, M., Karnieli, A., Ginat, H., Meiri, E., & Fredj, E., 2017. An innovative method for determining hydrological calibration parameters for the WRF-Hydro model in arid regions. *Environmental Modelling and Software 91*, 47–69. https://doi.org/10.1016/j.envsoft.2017.01.010

Skamarock, W.C., Klemp, J.B., Dudhia, J., Gill, D.O., Zhiquan, L., Berner, J., … Huang, X.-Y., 2019. A Description of the Advanced Research WRF Model Version 4. NCAR Tech. Note NCAR/TN-475+STR.

Sun, M., Li, Z., Yao, C., Liu, Z., Wang, J., Hou, A., … Liu, M., 2020. Evaluation of flood prediction capability of the WRF-hydro model based on multiple forcing scenarios. *Water* (Switzerland) *12*. https://doi.org/10.3390/w12030874

Team GHRSST, 2010a. Black Sea Ultra High Resolution SST L4 Analysis 0.01 deg Resolution | PO.DAAC / JPL / NASA. Available at: https://podaac.jpl.nasa.gov/dataset/OISST_UHR_NRT-GOS-L4-BLK-v2.0?ids=TemporalResolution&values=Daily&search=l4 [Accessed 7 January 2021].

Team GHRSST, 2010b. Mediterranean Sea Ultra High Resolution SST L4 Analysis 0.01 deg Resolution | PO.DAAC / JPL / NASA. Available at: https://podaac.jpl.nasa.gov/dataset/OISST_UHR_NRT-GOS-L4-MED-v2.0?ids=TemporalResolution&values=Daily&search=l4 [Accessed 7 January 2021].

Trenberth, K.E., 1999. Conceptual framework for changes of extremes of the hydrological

cycle with climate change. *Climate Change 42*, 327–339.

Turkes, M., 1999. Vulnerability of Turkey to desertification with respect to precipitation and aridity conditions. *Turkish Journal of Engineering and Environmental Sciences 23*, 363–380.

Turkes, M., 1996. Spatial and temporal analysis of annual rainfall variations in Turkey. *International Journal of Climatology 16*, 1057–1076. https://doi.org/10.1002/(SICI)1097-0088(199609)16:9<1057::AID-JOC75>3.0.CO;2-D

Turuncoglu, U.U., 2015. Identifying the sensitivity of precipitation of Anatolian peninsula to Mediterranean and Black Sea surface temperature. *Climate Dynamics 44*, 1993–2015. https://doi.org/10.1007/s00382-014-2346-7

Varlas, G., Anagnostou, M.N., Spyrou, C., Papadopoulos, A., Kalogiros, J., Mentzafou, A., … Katsafados, P., 2019. A multi-platform hydrometeorological analysis of the flash flood event of 15 November 2017 in Attica, Greece. *Remote Sensing 11*. https://doi.org/10.3390/rs11010045

Wang, J., Wang, C., Rao, V., Orr, A., Yan, E., & Kotamarthi, R., 2019. A parallel workflow implementation for PEST version 13.6 in high-performance computing for WRF-Hydro version 5.0: a case study over the midwestern United States. *Geoscientific Model Development 12*, 3523–3539. https://doi.org/10.5194/gmd-12-3523-2019

Wehbe, Y., Temimi, M., Weston, M., Chaouch, N., Branch, O., Schwitalla, … Al Mandous, A., 2019. Analysis of an extreme weather event in a hyper-arid region using WRF-Hydro coupling, station, and satellite data. *Natural Hazards and Earth System Sciences 19*, 1129–1149. https://doi.org/10.5194/nhess-19-1129-2019

Yang, Y., Yuan, H., & Yu, W., 2018. Uncertainties of 3D soil hydraulic parameters in streamflow simulations using a distributed hydrological model system. *Journal of Hydrology 567*, 12–24. https://doi.org/10.1016/j.jhydrol.2018.09.042

Yucel, I., & Onen, A., 2014. Evaluating a mesoscale atmosphere model and a satellite-based algorithm in estimating extreme rainfall events in northwestern Turkey. *Natural Hazards and Earth System Sciences 14*, 611–624. https://doi.org/10.5194/nhess-14-611-2014

Yucel, I., Onen, A., Yilmaz, K.K., & Gochis, D.J., 2015. Calibration and evaluation of a flood forecasting system: Utility of numerical weather prediction model, data assimilation and satellite-based rainfall. *Journal of Hydrology 523*, 49–66. https://doi.org/10.1016/j.jhydrol.2015.01.042

841

843 Table 1 Drainage areas and calibrated event periods of each selected basin over EBS and
844 MED regions.

Region	Station	Drainage Area (km^2)	Calibration Event Period	
			Start	End
EBS	D22A049	175.8	08/27/2016	09/06/2016
			09/20/2017	09/30/2017
			10/19/2016	10/29/2016
	D22A079	85.8	10/19/2016	10/29/2016
			10/01/2018	01/11/2018
			06/24/2019	07/04/2019
	D22A089	71.5	08/27/2016	09/06/2016
			09/20/2017	09/30/2017
			10/19/2016	10/29/2016
	D22A147	41.9	08/27/2016	09/06/2016
			09/20/2017	09/30/2017
			10/19/2016	10/29/2016
MED	D08A071	98.3	01/09/2015	01/19/2015
			03/07/2017	03/17/2017
			03/23/2015	04/02/2015
	E08A008	164.6	01/09/2015	01/19/2015
			03/07/2017	03/17/2017
			03/23/2015	04/02/2015
	D09A095	164.6	01/21/2014	01/31/2014
			01/09/2015	01/19/2015
			03/23/2015	04/02/2015

845
846
847
848

Table 2 SST products and initial boundaries included as meteorological forcings in the scope of this study and model run periods corresponding to EBS and MED region.

Region	Meteorological Forcings		Model Run Periods	
	SST Products	Initial and Boundary Conditions	Start Date	End Date
EBS	ECMWF GHR Medspiration NCEP	ERA5 Reanalysis	08/17/2015	08/27/2015
MED	GFS GHR Medspiration NCEP	GFS Forecast	12/10/2018	12/20/2018

Table 3 Average statistics of (Bias, Root Mean Square Error (RMSE), and Correlation Coefficient (RR)) calibrated parameters for three events compare to default parameter set for D22A049 and D22A147 basins over EBS region.

	D22A049				D22A147			
	Parm. Values	Bias	RMSE	RR	Parm. Values	Bias	RMSE	RR
Default Parameter Set		4.24	40.55	0.13		0.48	5.75	0.38
REFKDT	0.5	3.72	40.48	0.38	0.5	0.58	3.20	0.63
RETDEPRT	0.0	4.00	40.45	0.39	0.0	0.60	3.18	0.62
SLOPE	0.1	4.00	40.45	0.39	1.0	1.01	2.88	0.67
OVROUGHRTFAC	1.0	4.00	40.45	0.39	1.0	1.01	2.88	0.67
MANN	2.0	3.69	37.54	0.39	2.0	0.85	2.76	0.64
LKSATFAC	10	-2.34	32.16	0.56	10	0.55	2.33	0.71

Table 4 Average statistics of (Bias, Root Mean Square Error (RMSE), and Correlation Coefficient (RR)) calibrated parameters for three events compare to default parameter set for D08A071, D09A095 and E08A008 basins over MED region.

	D08A071				D09A095			
	Parm. Values	Bias	RMSE	RR	Parm. Values	Bias	RMSE	RR
Default Parameter Set		-5.28	16.67	0.44		2.78	17.02	0.45
REFKDT	0.5	-1.02	30.12	0.44	0.5	1.31	9.67	0.73
RETDEPRT	0.0	-0.47	30.53	0.44	0.0	5.28	16.58	0.42
SLOPE	0.1	-0.47	30.53	0.44	1.0	5.48	15.65	0.48
OVROUGHRTFAC	1.0	-0.47	30.53	0.44	0.1	1.69	8.55	0.70
MANN	2.0	-0.50	29.85	0.49	2.0	1.70	8.35	0.81
LKSATFAC	10	-5.57	26.30	0.46	10	2.29	9.02	0.77

	E08A008			
	Parm. Values	Bias	RMSE	RR
Default Parameter Set		12.22	15.98	0.25
REFKDT	0.5	11.81	15.38	0.39
RETDEPRT	0.0	11.80	15.35	0.39
SLOPE	0.1	11.80	15.35	0.39
OVROUGHRTFAC	1.0	11.80	15.35	0.39
MANN	0.5	11.84	15.19	0.37
LKSATFAC	10	2.52	4.23	0.31

881 Table 5 Default and calibrated parameter values for each basin.

Parameter	Default Parameter Value	Calibrated Parameter Value						
		EBS				MED		
		D22A049	D22A079	D22A089	D22A147	D08A071	D09A095	E08A008
REDKT	3.0	0.5	0.5	0.5	0.5	0.5	0.5	0.5
RETDEPRTFAC	1.0	0.0	0.0	0.0	0.0	0.0	0.0	0.0
SLOPE	0.1	0.1	0.1	1.0	1.0	0.1	1.0	0.1
OVROUGHRTFAC	1.0	1.0	1.0	0.1	1.0	1.0	0.1	1.0
MANN	1.0	2.0	2.0	2.0	2.0	2.0	2.0	0.5
LKSATFAC	1000	10	10000	1000	10	10	10	10

882

883

884

885

886

887

888

889

890

891

892

Table 6 Statistics of Bias, RMSE, and RR between observed and modelled precipitations with different SST datasets a) ECMWF, GHRSST, Medspiration, and NCEP for D22A147 over EBS and b) GFS, GHRSST, Medspiration, and NCEP for D08A071 over MED are shown.

Station	SST WRF Runs	Bias	RMSE	RR
D22A147	ECMWF-SST	-0.54	3.19	0.03
	GHR-SST	-0.06	5.30	0.01
	MED-SST	-0.24	3.55	0.03
	NCEP-SST	-0.54	3.38	0.01
D08A071	GFS-SST	0.56	3.45	0.60
	GHR-SST	0.18	2.35	0.52
	MED-SST	0.13	1.86	0.67
	NCEP-SST	0.33	2.23	0.60

Table 7 Statistics of Bias, RMSE, and RR between observed and modelled hydrographs of D22A147 and D08A071 for SST events over EBS and MED regions.

Station	SST WRF-Hydro Runs	Default Parameter Set			Calibrated Parameter Set		
		Bias	RMSE	RR	Bias	RMSE	RR
D22A147	ECMWF-SST	-10.46	20.69	0.29	-9.92	20.13	0.42
	GHR-SST	-8.71	16.49	0.83	-6.16	10.82	0.83
	MED-SST	-10.24	20.13	0.86	-8.32	15.86	0.86
	NCEP-SST	-10.42	20.55	0.83	-9.60	18.98	0.82
D08A071	GFS-SST	-7.07	125.97	0.30	-24.98	128.81	0.18
	GHR-SST	-26.56	57.30	0.62	-42.73	83.25	0.30
	MED-SST	-26.24	59.70	0.59	-43.63	83.57	0.31
	NCEP-SST	-18.85	58.79	0.60	-40.76	81.50	0.32

FIGURE LEGENDS

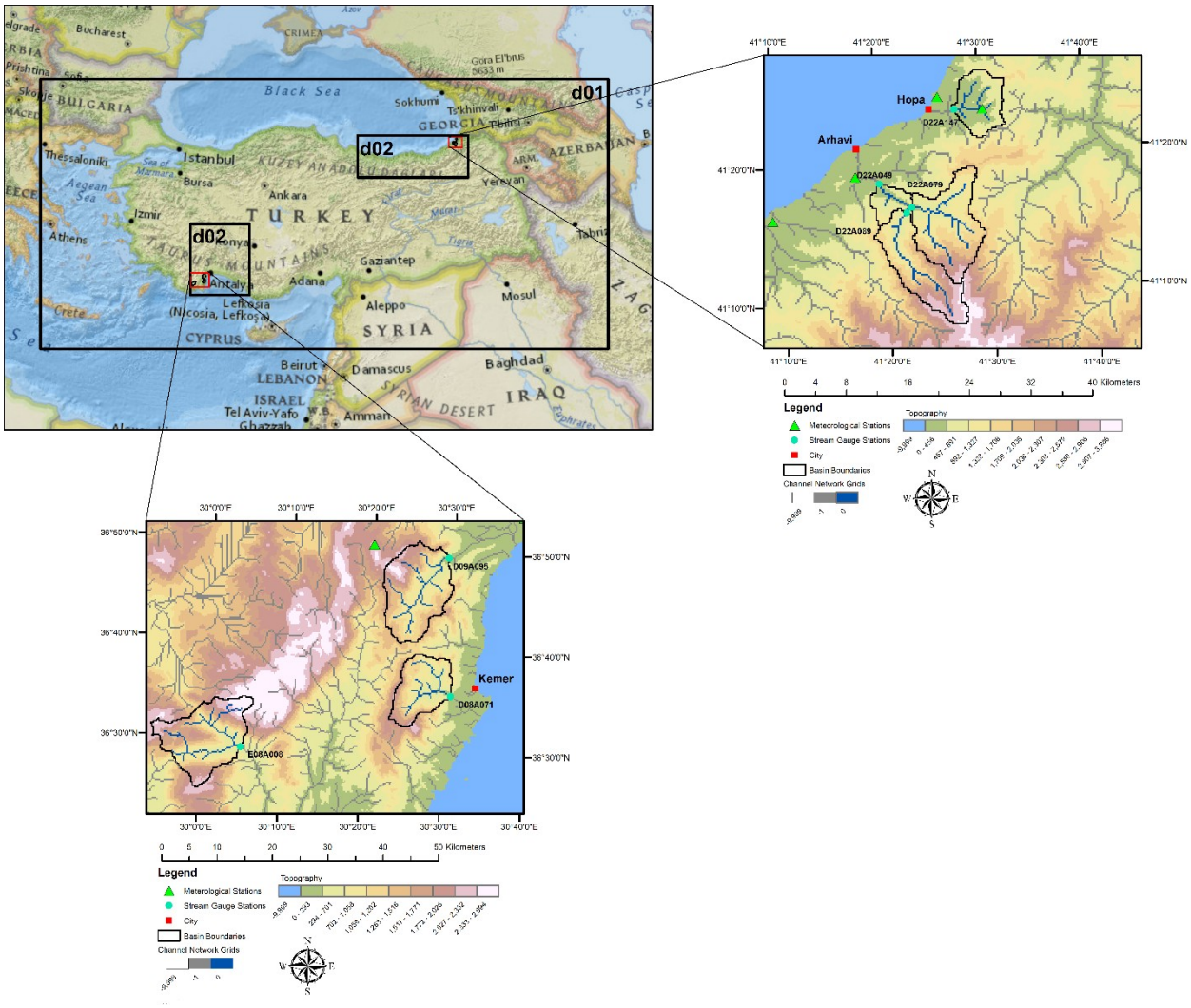

Figure 1 The outer and nested domains (d01 and d02) of the WRF model for EBS and MED regions are displayed in the top-left. Boundaries of the selected basin, their outlet points (stream gauge stations denoted as blues dots), channel network grids in the WRF-Hydro model, and the meteorological station (denoted as a green triangle) are shown in the zoomed maps with the high-resolution topography layer at the background.

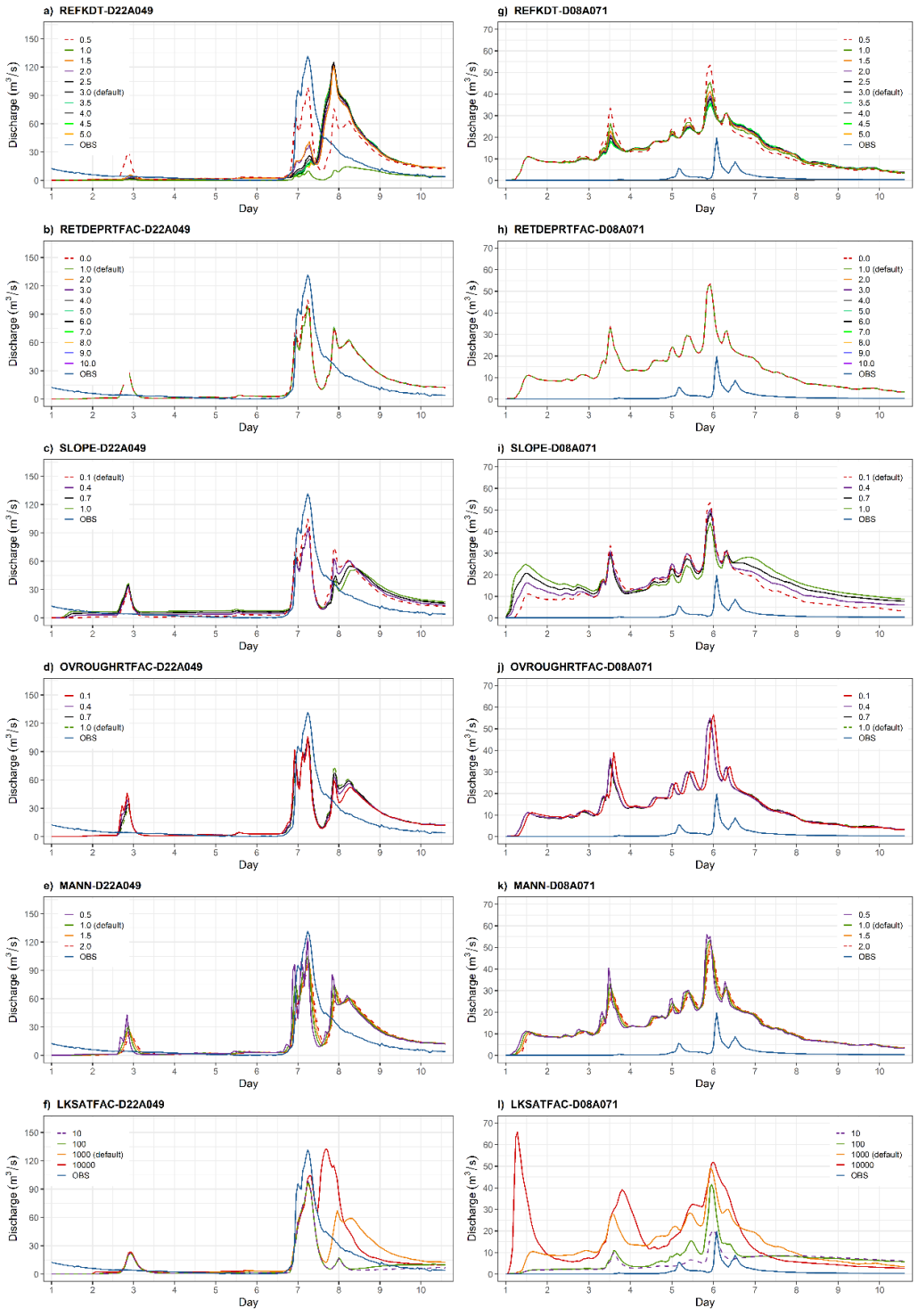

Figure 2 Calibration results of the selected WRF-Hydro model parameters, namely REFKDT, RETDEPRT, SLOPE, OVROUGHRTFAC, MANN, and LKSATFAC: a-f) left column for event occurred between 10/19/2019 to 10/29/2016 and basin D22A049 located over EBS region; g-l) right column for event occurred between 03/07/2017 to 03/17/2017 and basin D08A071 located over MED region. Dashed line shows the hydrograph for selected optimum parameter value.

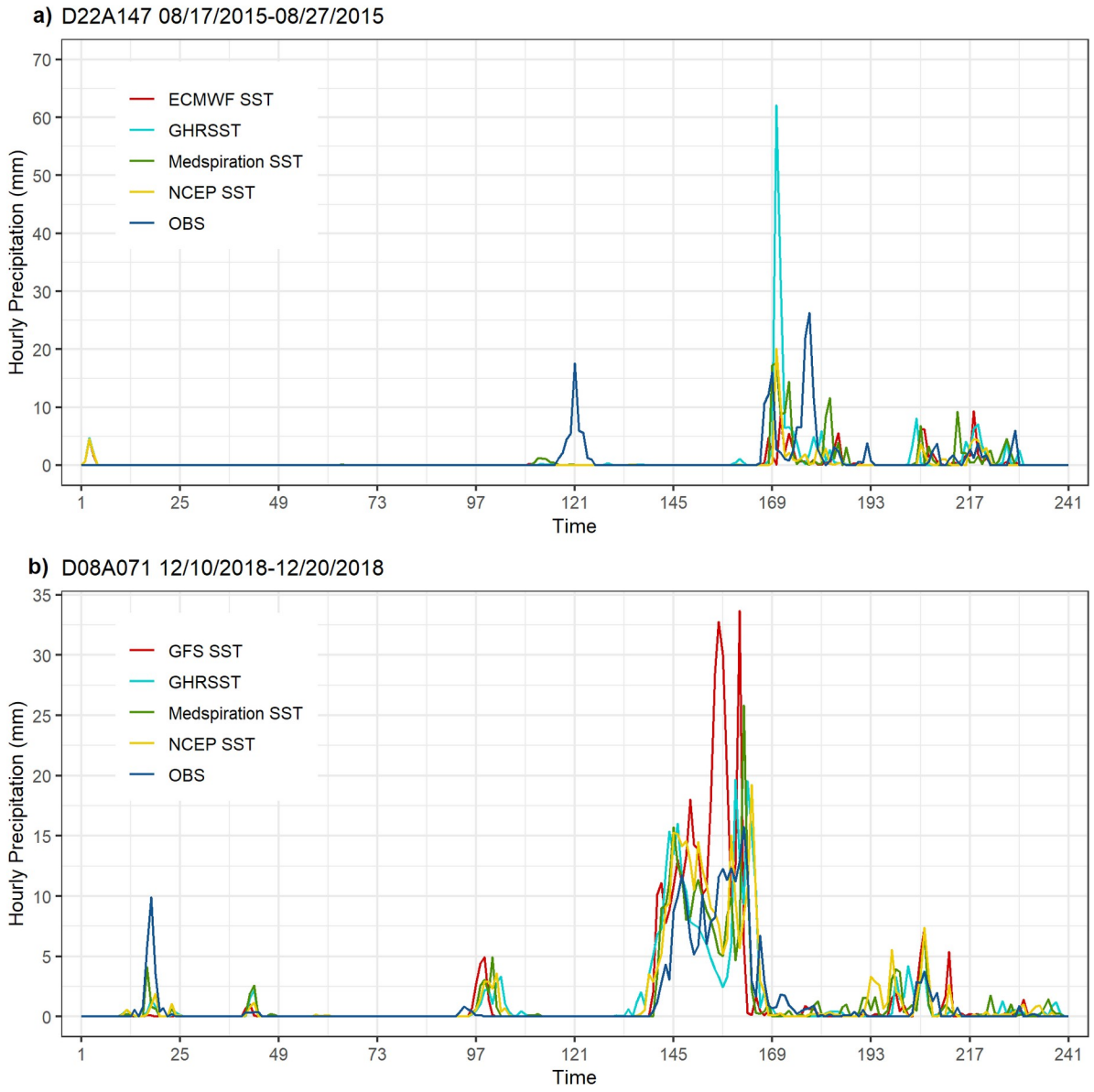

941

942 Figure 3 Time series of hourly precipitation that a) D22A147 basin over EBS region receives
943 during the event occurred in 08/17/2015-08/27/2015 and b) D08A071 basin over MED region
944 receives during the event occurred in 12/10/2018-12/20/2018 for 10 days. Outputs are
945 generated from WRF model with the native SST field from ERA5 Reanalysis data (ECMWF-
946 SST) for EBS region and GFS Forecast data (GFS-SST) for MED region with different SST
947 products: GHRSST, Medspiration, and NCEP.

948

949

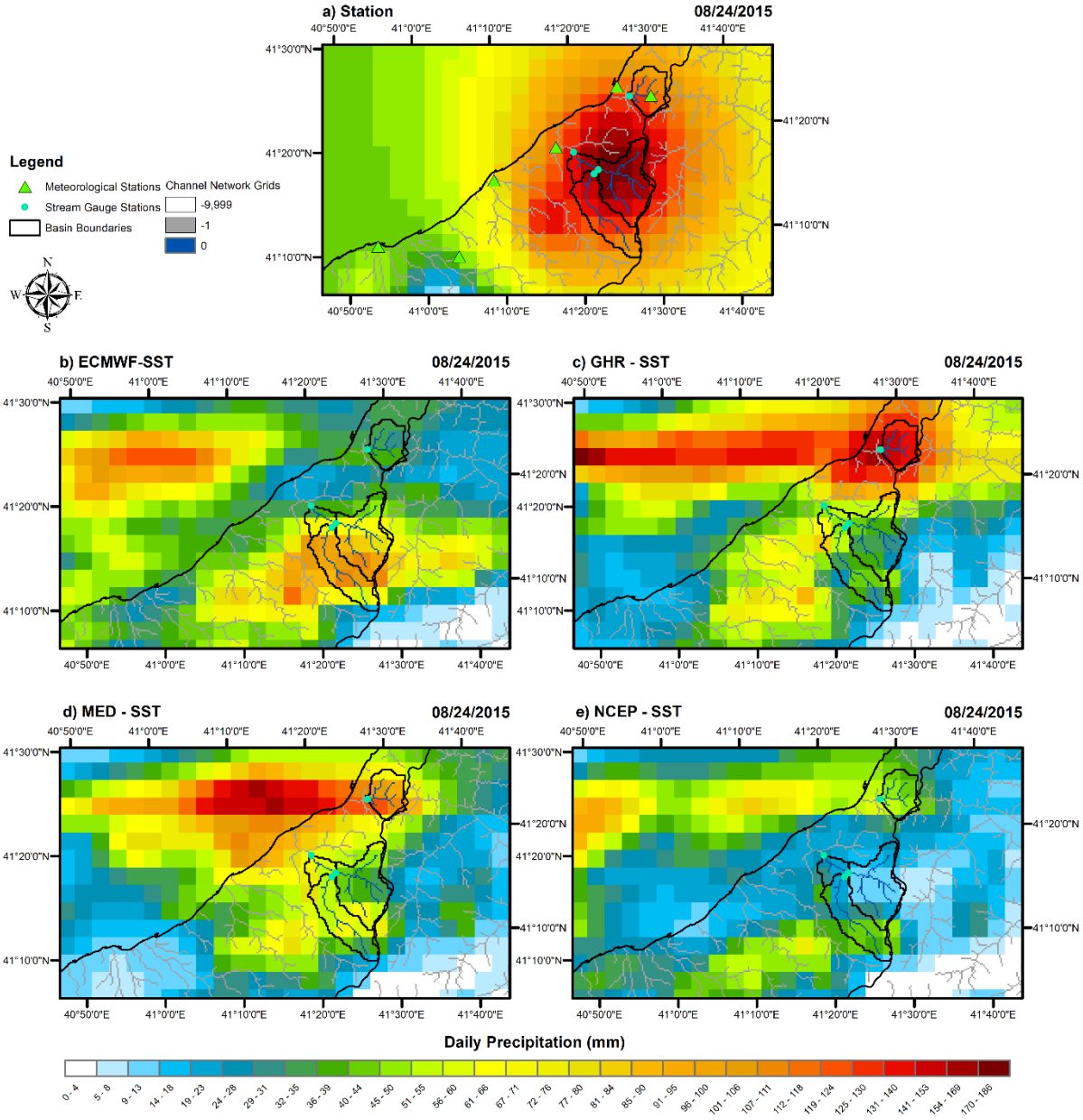

Figure 4 Spatial distribution of daily precipitation at the peak day (08/24/2015) for run period of 08/17/2017 – 08/27/2017 over EBS region. a) The map at the top shows the interpolated observed precipitation map obtained from meteorological stations data (green triangles). Black line indicates the boundaries of selected basins for this study while blue dots show the corresponding stream gauge stations. The four maps at the sub-panels refer the simulated precipitations by WRF model derived by different SST data sources for the peak hour: b) GFS, c) GHRSST, d) Medspiration and e) NCEP, respectively

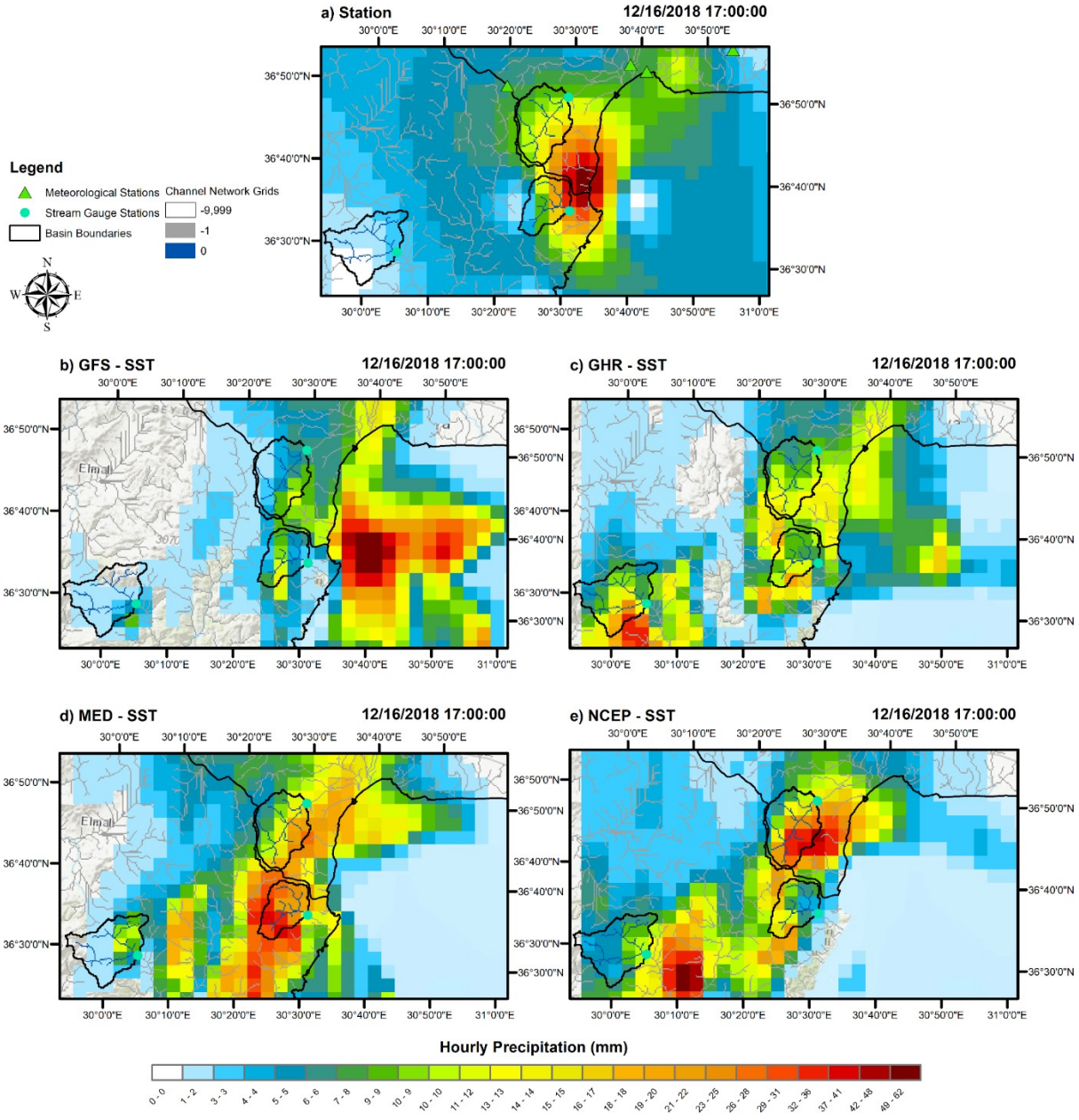

960

961 Figure 5 Spatial distribution of hourly precipitation at the peak hour (12/16/201817:00:00
962 UTC) for run period of12/10/2018–12/20/2018 over MED region. a) The map at the top
963 shows the interpolated observed precipitation map obtained from meteorological stations data
964 (green triangles). Black line indicates the boundaries of selected basins for this study while
965 blue dots show the corresponding stream gauge stations. The four maps at the sub-panels
966 refer the simulated precipitations by WRF model derived by different SST data sources for
967 the peak hour: b) GFS, c) GHRSST, d) Medspiration and e) NCEP, respectively.

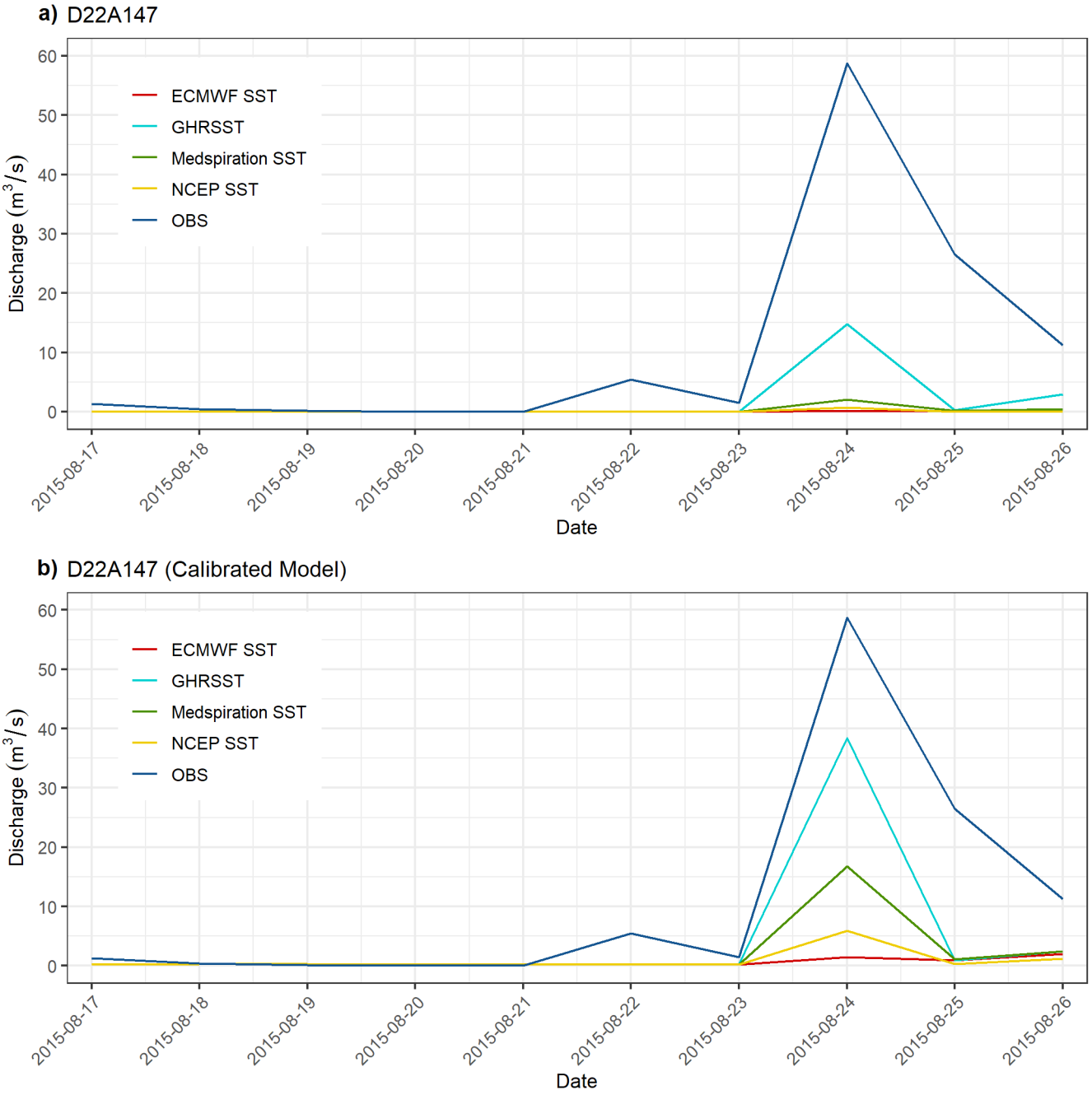

968

969 Figure 6 Comparison of observed hydrographs with the simulated hydrographs generated
970 using precipitation inputs derived with native SST field (ECMWF), GHRSST, Medspiration
971 and NCEP a) prior to the calibration and b) with the calibrated parameter set of the WRF-
972 Hydro model for event 08/17/2015-08/27/2015 in D22A147.

973

974

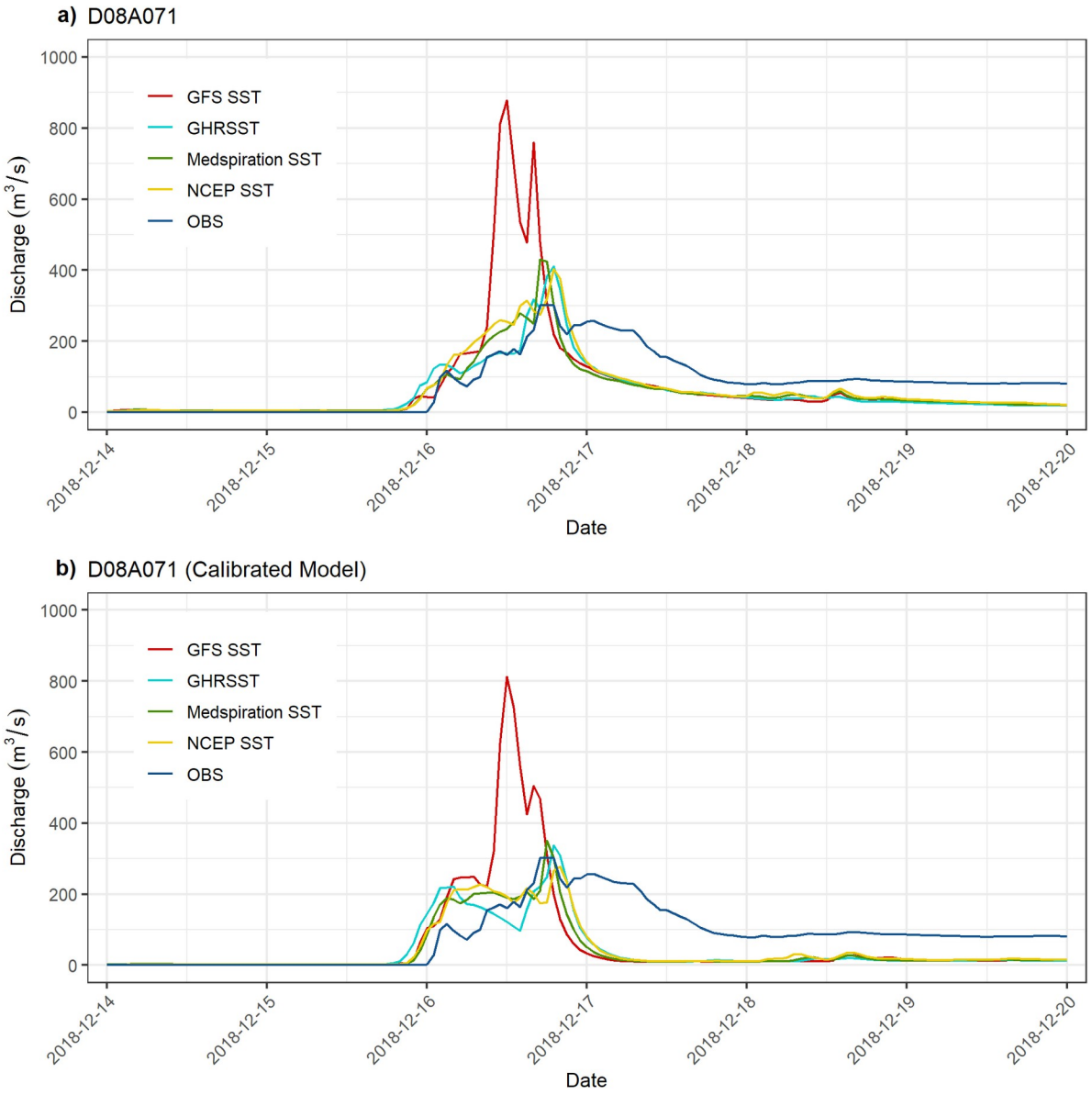

975

976 Figure 7 Comparison of observed hydrographs with the simulated hydrographs generated
977 using precipitation inputs derived with native SST field (GFS), GHRSST, Medspiration and
978 NCEP a) prior to the calibration and b) with the calibrated parameter set of the WRF-Hydro
979 model for event 12/10/2018-12/20/2018 in D08A071.

980

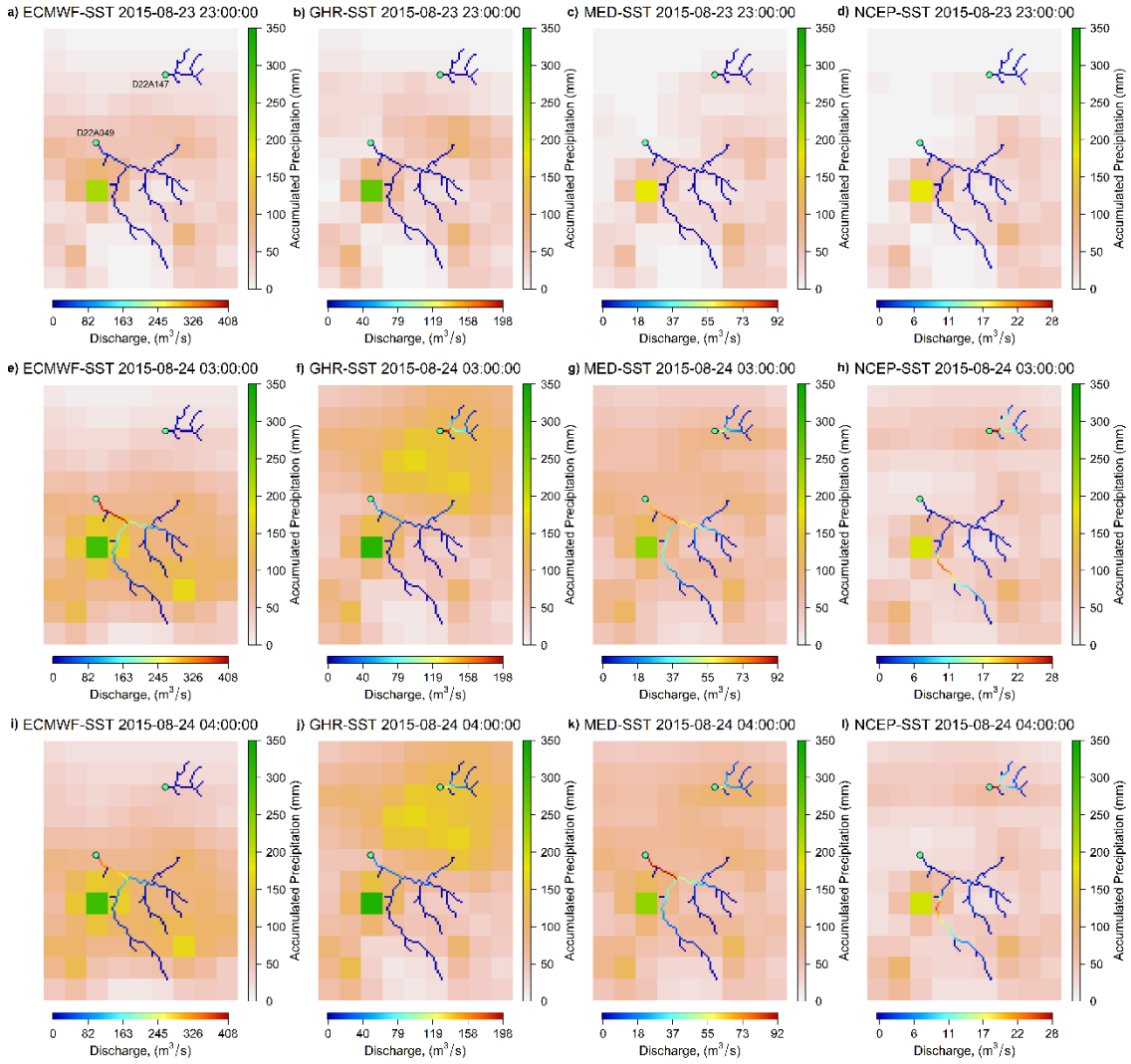

981

982 Figure 8 Overlapped dynamic maps of accumulated precipitation simulated by WRF model
983 (3-km) operated with 4 different SST datasets (ECMWF, GHRSST, Medspiration and NCEP)
984 and discharge simulated by WRF-Hydro model (250-m) over EBS region at 08/23/2015
985 23:00:00, 08/24/2015 03:00:00, and 08/24/2015 04:00:00. Stream gauges are denoted as
986 blued dots.

987

988

989

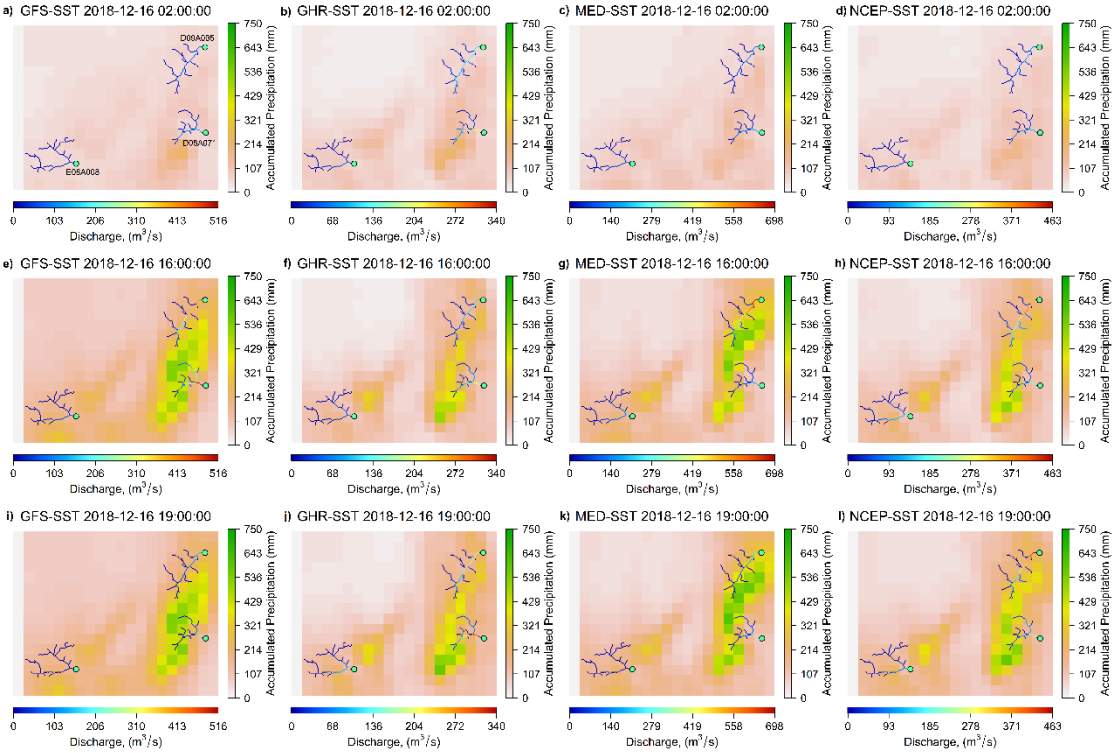

990

991 Figure 9 Overlapped dynamic maps of accumulated precipitation simulated by WRF model
992 (3-km) operated with 4 different SST datasets (GFS, GHRSST, Medspiration and NCEP) and
993 discharge simulated by WRF-Hydro model (250-m) over MED region at 12/16/2018
994 02:00:00, 12/16/2018 16:00:00, and 12/16/2018 19:00:00. Stream gauges are denoted as
995 blued dots.

996

997

998

999

1000

1001

1002

1003